Materials Science-Poland, 41(2), 2023, pp. 325-338
http://www.materialsscience.pwr.wroc.pl/
DOI: 10.2478/msp-2023-0024

sciendo

Improving optical and morphological properties of Mn-doped ZnO via Ar ion sputtering followed by high-temperature UHV annealing

Elhachemi Zehar[1,*], Abdallah Ouerdane[2], Boualem Chetti[2], Ali Çoruh[3]

[1]Laboratory of Energy and Smart Systems, Faculty of Science and Technology, University of Khemis Miliana 44225, Algeria
[2]University of Khemis Miliana 44225, Algeria
[3]Department of Physics 54147-Kampus Sakarya-Turkey

Using the ultrasonic spray pyrolysis technique, pure (ZnO) and manganese (4at%)-doped zinc oxide (ZnMnO) thin films were synthesized and treated with Ar^+ sputtering in the UHV (ultra-high vacuum) system. In this regard, XRD (X-ray diffraction), XPS (X-ray photoelectron spectroscopy), PL (photoluminescence), and AFM (atomic force microscopy) techniques were applied to investigate the electronic and photonic properties of ZnO. XRD and XPS allowed us to identify the successful incorporation of Mn as a substitute for Zn, while PL and AFM images reveal a high tendency for crystalline grains on theZnMnO surface to aggregate to form small grains. However, bandgap narrowing, a redshift with considerable fluctuations in excitonic emission, and a perfect quenching of visible emission (400–640 nm) were observed. Investigations into defect-related emission in ZnMnO and ZnO compounds were conducted. The PL spectra of the prepared samples were measured and analyzed using Gaussian fitting. The PL of undoped ZnOexhibited an intense broad band with a peak at 550 nm. Two effects were shown to occur as a result of Mn doping: (i) a sharp quenching of self-activated PL with a progressive red-shift of the quenching's spectral boundary; (ii) the appearance of a new emission band with a peak at 1.64 eV (756 nm), which dominates the PL spectrum and is noted in a band diagram; as well as a slight shift in the main line of ZnO, which is located at energy 3.275 eV (378.57nm).

Keywords: *characterization, ZnMnO, optical, Mn incorporation, morphological, defects, band diagram*

1. Introduction

Due to its exceptional electronic and optical properties, including a substantial exciton binding energy of 60 meV and a wide band gap energy of 3.37 eV at room temperature, zinc oxide (ZnO) has garnered significant interest as a transparent conductor oxide (TCO). This versatile material finds applications in various fields, such as gas sensors [1], catalysts [2–6], photovoltaic solar cells [7], supercapacitors [8], and flexible piezoelectric nanogenerators [9]. Numerous researchers have dedicated their efforts to exploring the effect of doping on ZnO, aiming to enhance its optical, electrical, and magnetic characteristics. Incorporating minute quantities of dopant metal oxide materials, such as Mn^{2+}, Mg^{2+}, Sb^{3+}, In^{3+}, Cu^{2+}, Co^{3+}, Al^{3+}, and others [10–18], represents the primary approach to synthesizing ZnO alloys with widened band gaps in various nanostructures, including nanofibers, nanocônes, nanowires, and more [19–21].

Transition metal (TM) ion-doped zinc oxide (ZnO) has gained significant scientific interest due to its remarkable properties and potential for spintronic applications, where the coexistence of electron spin and charge plays a crucial role.The strong correlation between the "3D" orbital of transition metals and the "s" and "p" orbitals of the anion profoundly alters the electronic structure of the ZnO host lattice. Consequently, ZnO-based dilute magnetic semiconductors (DMS) have emerged as a promising class of materials, surpassing conventional semiconductors in their potential applications [22, 23]. Extensive research efforts have focused on incorporating transition metals like Mn, Fe, Co, Cu, Ni, Cr, and V as substitutional ions in

* E-mail: z.hachemi@univ-dbkm.dz

the ZnO lattice to achieve ferromagnetic properties at or above room temperature.

Manganese (Mn^{2+}) is distinguished among the various TM elements because of its notable thermal solubility in ZnO [24]. With its half-filled 3D orbitals housing five spins, Mn^{2+} exhibits a maximum moment value of 5μB/Mn (where μB represents the Bohr magneton) [25]. Despite the difference in ionic radii between Mn^{2+} (0.083 nm) and Zn^{2+} (0.074 nm) and the limited solubility of approximately 13% in the ZnO matrix [25], extensive studies confirm that manganese ions can effectively substitute for zinc ions without inducing distortion in the ZnO lattice. At low concentrations (1%–5%), this substitution process provides favorable properties such as homogenous grain shape, solid texture, and improved crystallinity [6, 26–28]. Consequently, ZnMnO thin films prove to be an ideal material for short-wavelength magneto-optical applications.Currently, a variety of techniques are employed for the synthesis of ZnO nanomaterials, including hydrothermal methods [29–31], solution processing [32], pulsed laser deposition [33], and pyrolysis sputtering [10, 13, 34]. Among these approaches, pyrolysis is favored in this study because of its convenience of use, nonvacuum, good homogeneity, and cost-effectiveness. Moreover, as a critical phase in the development of reliable devices, the ZnMnO samples undergo Ar^{+} ion sputtering [35], followed by a precisely controlled thermal annealing process within the ultra-high vacuum (UHV) system [36]. Prior to treatment, the ZnO samples are investigated using XRD, XPS, AFM, and PL techniques, while the ZnMnO samples are examined both before and after treatment.

The aim of this research is to explore the impact of a 4% Mn dopant and investigate how cleaning and thermal annealing processes (Ar^{+} sputtering followed by high-temperature UHV annealing) affect the structure, morphology, and optoelectronic properties of ZnMnO film. Furthermore, establish a correlation between the electronic band gaps, band transitions, and the structural and morphological characteristics of these thin films.

2. Experimental section

2.1. Preparation process

On a silicon (Si) substrate, thin films of pure ZnO and ZnMnO (4at% Mn) were prepared using the ultrasonic spray pyrolysis technique. Zinc acetate dehydrates ($ZnC_4H_6O_4\_2H_2O$) (99%, Sigma Aldrich) were dissolved in 100 ml of methanol at a molar concentration of 0.4 mol/l to produce ZnO. Manganese chloride tetrahydrate ($MnCl_2$ $4H_2O$) (Sigma Aldrich, 98%) is used as a dopant to create ZnMnO. The precursor solution contains 4% of Mn as the molar ratio concentration $|Mn|/(|Mn|+|Zn|)$. To make sure the two solutions are homogeneous, they are each stirred for one hour at 40°C.The elaboration procedure was succeeded by spraying the precursor solutions over the heated substrates for 60 min at a temperature of 400°C.

2.2. Treatment process

Using a Scientaomicron UHV system with a preparation chamber and an analysis chamber, thin films of manganese-doped ZnO at 4% Mn were created. The samples were transported into the preparation or analysis chamber by a magnetically coupled probe transporter, and each chamber was pumped separately using manual or electropneumatic gate valves. When it comes to cleaning, an ion gun with a pulverized source is used to bombard the samples' surfaces in order to get rid of different contaminants like carbon and oxygen that are on the surface layer. The cathodic sputtering ion source's low energy is sufficient to produce flawless cleaning. It should be noted that the pressure of Ar^{+} ion gas released by a leaky valve becomes 2.10^{-6} mbar. With a low ion current of 3 A, the energy is fixed at 1.2 keV for 15 min. Using a standard manipulator and a pyrolytic boron nitride (PBN)-resistive device, the heating process was conducted in steps of increasing temperature (from 350°C up to 800°C) for 20 min at a time.

2.3. Characterization details

To study the structural properties, the EMPYREAN Diffractometer System was employed for conducting X-ray diffraction (XRD)

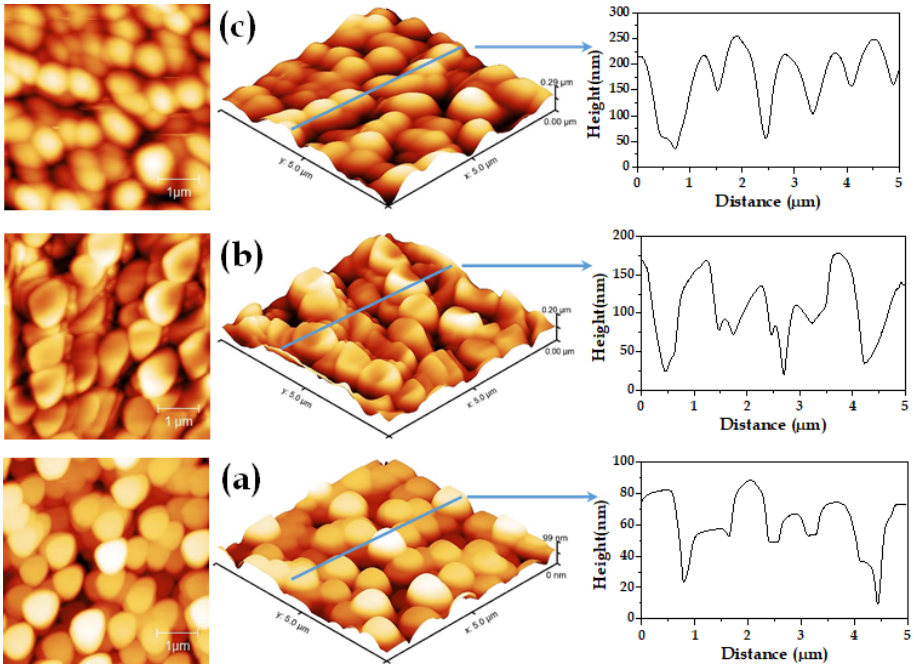

Fig. 1. 2D and 3D topographic AFM images accompanied by curves of line profiles corresponding to pure ZnO (a), untreated *ZnMnO* (b), and treated *ZnMnO* (c)

analysis on ZnO and ZnMnO thin films. Operating at 45 kV and 40 mA, the system utilizes CuKα radiation (λ = 1.54060 Å) to capture the XRD spectrum within the angular range of 10° to 66°, employing a step size of $2\theta^\circ$ = 0.02°. To obtain X-ray photoelectron spectra (XPS) of the samples, a dual-anode X-ray source (DAR400) [31] was utilized. The XPS spectra were acquired by exciting the samples with monochromatic Mg-Kα (1253.6 eV) radiation. The anode voltage was set to 15 kV, and the emission current was maintained at 15 mA, corresponding to a power of 225 W. Casa-XPS software was used to calculate the atomic concentrations (at.%) of the chemical elements present on the surface. For the characterization of surface morphology and roughness, the Flex-Axiom Nanosurf atomic force microscope (AFM) was employed. Gwyddion data analysis software was utilized to process the topographic images obtained from the AFM measurements. For the purpose of investigating the presence of defects,photoluminescence (PL) measurements were carried out at room temperature using the HORIBA iHR-550 spectrometer. The measurements were conducted within the wavelength range of 340–1040 nm, and a power of 30 mW was carefully chosen as the excitation source to ensure its suitability for effectively exciting wide bandgap semiconductors.

3. Results and discussion

3.1. AFM result

Figure 1 exhibits the line profiles of ZnO and ZnMnO, accompanied by the 2D and 3D AFM images, denoting pure ZnO (a), untreated ZnMnO (b), and treated ZnMnO (c), respectively. The surface morphology of ZnMnO differs significantly from that of ZnO, necessitating a precisely controlled treatment procedure involving Argon ion (Ar^+) beam sputtering [37], followed by thermal annealing [38]. The purpose of this treatment is to enhance surface roughness and diminish grain size. Notably, Figure 1c illustrates the outcome of this process. Roughness, a parameter associated with geometric defects on the actual surface, serves as an informative indicator of the adhesion and surface conditions of the deposited layers. ArzuÇolak,

Table 1. The main statistical parameters calculated through the AFM images in Figure 1 using Gwyddion software

Sample	Maximum height (Z_{max}) (nm)	Median height (Z_{med}) (nm)	Mean roughness (Sa) (nm)	Number of grains (N)
ZnO	98.84	60.22	13.50	115
Untreated *ZnMnO*	198.0	106.46	27.05	152
Treated *ZnMnO*	288.84	132.52	43.03	126

Zandvliet, and Poelsema [39] previously conducted comprehensive assessments of adhesion force in relation to surface morphology and power spectral density on both smooth and etched surfaces. Additionally, this technique facilitates the determination of particle size and the distance between different grain boundaries [40]. The AFM images are substantiated quantitatively in terms of Ra (average roughness), Rms (root mean square), maximum height (Z_{max}), and median height (Z_{med}), all acquired from the topographic information rendered by the atomic force microscope maps. A summary of these findings is presented in Table 1. Manganese has a significant effect on the atomic arrangement, forming small, well-resolved crystal grains on the ZnMnO surface. In addition, UHV treatment significantly improves the morphology of ZnMnO, as inferred from the mean roughness Sa calculated using Gwydion software (43.03 nm and 13.5 nm for pure ZnO and ZnMnO, respectively). Importantly, the maximum value of 288.84 observed in ZnMnO grains surpasses that of pure ZnO by threefold. This discovery holds profound significance since a rough surface optimizes the conversion of light, thereby heightening the efficiency of solar cells [41].

3.2. XRD results

Figure 2 illustrates the XRD patterns obtained for the two samples. The diffraction peaks of pure ZnO and treated ZnMnO exhibit well-matched indexing with the würtzite crystal structure (space group P63mc) [JCPDF card 36-1451], with preferable orientation along (002). This suggests that the synthesized ZnO crystals are predominantly aligned along the c-axis. Moreover, it is worth mentioning that the c/a values closely resemble those of the ideal würtzite structure ($\frac{c}{a} = \sqrt{\frac{8}{3}}$).

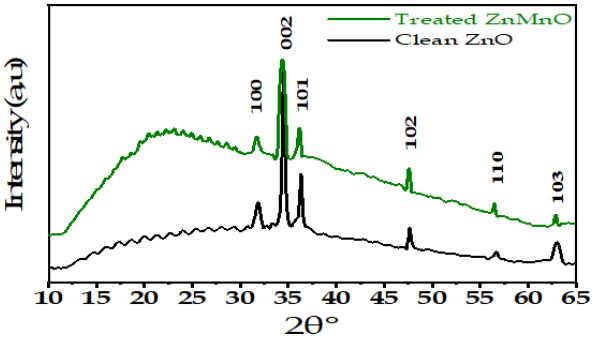

Fig. 2. XRD spectra of undoped ZnO and treated *ZnMnO* With six pics (100), (002), (101), (102), (110) and (103)

Figure 2 shows fluctuating disturbance halos appearing on the diffraction spectrum above (hump) and below (hollow) the line representing the noise contained in the diffraction. The spectra of the two ZnO and ZnMnO samples are located in the two regions: 2θ (30°–32.5°) and (37.5°–47.5°), repectively. This appearance is caused, as indicated by other authors [42, 43], by amorphous materials emerging during heat treatment undergone by the two samples during the processes of their successive elaborations. Such treatment forms ultra-thin layers of silicon oxide. or silicate for the as-prepared ZnO. Moreover, it can be seen that these halos become more pronounced and wider for the ZnMnO samples. This increase in dimensions is-due to the addition of an ultra-thin layer of manganese oxide. MnO or Mn_2O_3 on the surface of the manganese-doped ZnO sample.

The XRD analysis reveals that the ZnMnO crystal is free from any additional phases or impurities. Interestingly, the major peaks observed in the XRD pattern of ZnMnO show a slight shift towards lower angles compared to pure ZnO. This shift suggests a minor expansion of the unit cell in the ZnMnO sample. Consequently, the calculated lattice param-

Table 2. Structural parameters of ZnO and treated *ZnMnO*: tabulated XRD spectroscopy results

Sample	Peak position ($2\theta^\circ$)	h k l	FWHM ($2\theta^\circ$)	d-spacing (Å)	Average grain size D (nm)		Cell parameters (Å)		c/a	Strain (ε)	
					Scherrer equation	W-H Plot	$a=b$	c		Scherrer equation	W-H Plot
ZnO(0%)	31.84	1 0 0	0.58	2.80	25.20	28.88	3.242	5.195	1.602	0.0014	0.00085
	34.50	0 0 2	0.33	2.60							
	36.32	1 0 1	0.30	2.47							
	47.65	1 0 2	0.33	1.90							
	56.68	1 1 0	0.36	1.62							
	63.02	1 0 3	0.83	1.47							
ZnMnO(4%)	31.70	1 0 0	0.56	2.82	12.41	12.38	3.256	5.212	1.600	0.0025	0.00122
	34.38	0 0 2	0.67	2.60							
	36.17	1 0 1	0.36	2.48							
	47.56	1 0 2	0.29	1.91							
	56.44	1 1 0	0.21	1.63							
	62.87	1 0 3	0.30	1.47							

eters for ZnMnO are slightly larger than those for undoped ZnO. These findings strongly suggest the successful incorporation of Mn^{2+} ions (with an ionic radius of 0.83 Å) into the Zn^{2+} lattice sites (with an ionic radius of 0.74 Å). The findings of the XRD analysis are summarized in Table 2, which provides the position peaks ($2\theta^\circ$), corresponding diffraction planes, and the corresponding d_{hkl} interplanar spacing. Notably, these results demonstrate a high level of consistency with similar XRD studies conducted on Mn-doped ZnO films synthesized through spray pyrolysis [44–49].

Moreover, the average grain size (D) is determined through the XRD spectroscopy study by calculating it as a function of the broadening of the highest intensity peak corresponding to the diffraction plane (002). This calculation utilizes Debye Scherer's formula, as given in Eq. 1 [50].

$$D = \frac{0.9\lambda}{\beta\,(rd)\cos\theta} \tag{1}$$

Where λ is the X-ray wavelength (Cu-Kα: 1.5406 A°), β (rd) is the full width-half-maximum (FWHM), and θ (rd) is the peak position. The lattice parameters (a, c, and c/a) were calculated using formula (2):

$$\frac{1}{d_{hkl}^2} = \frac{4}{3}\left(\frac{h^2+hk+k^2}{a^2}\right) + \frac{l^2}{c^2} \tag{2}$$

Where d_{hkl} is the interplanar spacing determined by Bragg's law and h, k, and l are the Miller indices. the strain (ε) in the film is calculated using the following formula:

$$\varepsilon = \frac{\beta\,(rd)\cos\theta}{4} \tag{3}$$

The particle size of pure ZnO measures 25.20 nm, whereas the crystallite size of ZnMnO demonstrates a significant reduction to 12.41 nm. This decrease can be attributed to the enhanced solubility of Mn in ZnO, as observed in the study by Staumal et al. [51]. Additionally, it is important to note that the material experiences an increase in strain. This change arises from multiple factors, including the exchange of ions with different ionic radii, shifts in lattice constants, the introduction of impurities or defects, and the thermal extinction coefficient between the substrate and the film [52].

Figure 3 depicts the variance in $\beta_T\cos(\theta)$ vs. 4Sin(θ) (Williamson–Hall analysis) [53]. Equation (4) depicts (in linear form) y=mx + c, where

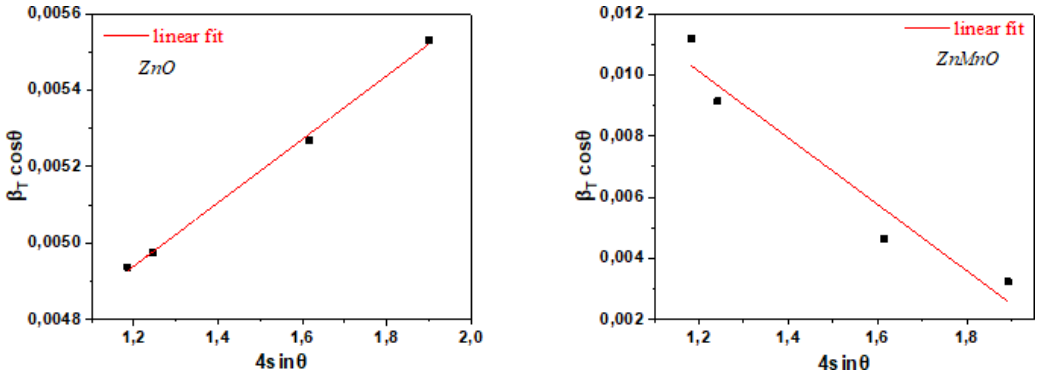

Fig. 3. Size-strain analysis (W-H plot) for ZnO and ZnMnO

m = strain and c = Kλ/D, such that the slope of the linear plot of cos(θ) versus Sin(θ) is lattice strain ε, and the intercept is Kλ/D.

$$\beta_T \cos\theta = \varepsilon\,(4\sin\theta) + \frac{K\lambda}{D} \qquad (4)$$

The W-H analysis for grain size look comparable; however, the results for strain appear to be widely off. These findings are consistent with the results obtained from the AFM study, providing further support for the notion that the diminished crystallite size predominantly stems from the distortion of the ZnO host lattice caused by the presence of Mn impurities. Consequently, this distortion facilitates accelerated crystal growth and the amalgamation of crystal grains.

3.3. XPS results

This study utilizes X-ray photoelectron spectra (XPS) to investigate the impact of Mn incorporation and UHV treatment on the chemical composition of ZnO thin films. Representative XPS results of clean ZnO and ZnMnO(untreated, sputtered, and annealed) are showcased in Figure 4(a). Notably, all photoelectron peaks (Zn 2p, Mn 2p, O 1s, C 1s, Zn 3s, Zn 3p, and Zn 3d) and Auger transition peaks (C-KLL, O KLL, and Zn LMM) associated with ZnO or ZnMnO materials are accurately identified. For data correction, the C 1s peak, located at 284.6 eV, is utilized as a reference. The atomic percentages (at%) of oxygen, manganese, and zinc elements are derived from the O 1s, Mn $2p_{3/2}$, and Zn $2p_{3/2}$ signals and are presented in Table 3. Figure 4(b) reveals a noteworthy observation that the C1s carbon signal is more pronounced in ZnMnO-compared to clean ZnO. Furthermore, the untreated ZnMnO exhibits a more significant C1s carbon signal than the annealed ZnMnO.

In Figure 4(c), the presence of the Zn 2p core level, which represents the divalent state of zinc ions in ZnO, is confirmed. The Zn $2p_{3/2}$ (1021.90 eV) and Zn $2p_{1/2}$ (1044.91 eV) photoelectron peaks exhibit a double peak energy separation of 23.01 eV, consistent with previous studies [54, 55]. However, when 4% Mn doping is introduced, the ZnMnO signals of Zn $2p_{3/2}$ and Zn $2p_{1/2}$ become less resolved due to the presence of a carbon contamination layer on the surface [56, 57]. Notably, following UHV treatment of ZnMnO, there is a substantial increase in the intensity of the Zn 2p signals, accompanied by a shift towards lower binding energies (approximately 0.45 eV) [58]. This observed shift could be attributed to morphological changes, as illustrated by the AFM images.

Figure 4(e) presents the high-resolution Mn 2p spectra, revealing prominent peaks at binding energy values of 641.8 eV and 653.9 eV, which correspond to Mn $2p_{3/2}$ and Mn $2p_{1/2}$, respectively. Interestingly, the Mn 2p signals exhibit negligible intensity in the contaminated state. However, upon subjecting the samples to UHV treatment, a notable improvement in peak shapes was observed.

Gaussian deconvolution was employed to explore the distribution of the Mn element within the thin films. As shown in Figure 5(a), the presence of distinct peaks at 641.10 eV and 653.0 eV provides unequivocal evidence for the existence of Mn^{2+}

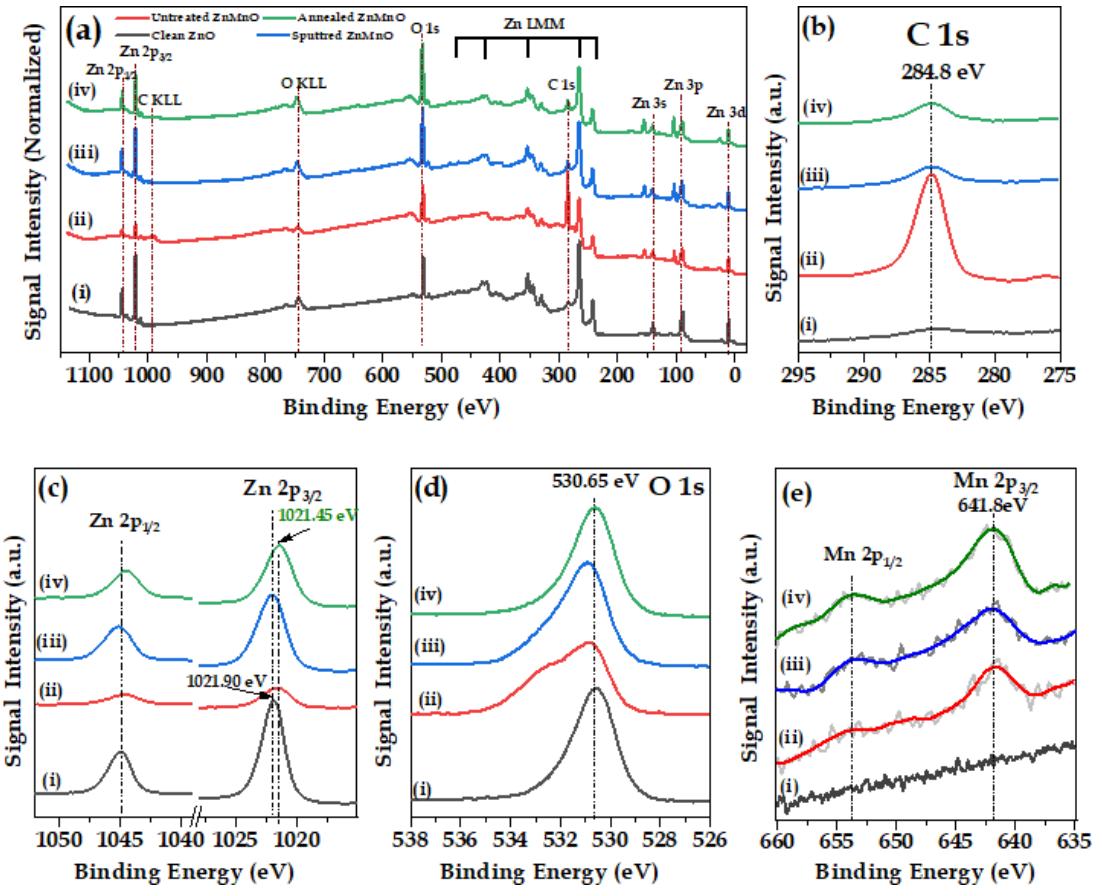

Fig. 4. XPS spectra of pure ZnO (i), initial *ZnMnO* (ii), *ZnMnO* post Ar ion sputtering (iii), and *ZnMnO* post Ar annealing at 800°C (iv). (a): full scan spectra. (b), (c), (d), and (e): narrow scan spectra corresponding to C 1s, doubled Zn 2p, O 1s, and doubled Mn 2p, respectively

Table 3. Atomic percentages of Zn, O, and Mn elements corresponding to pure ZnO and treated *ZnMnO*. (a) atomic ratio of the Mn atoms taking the Zn sites. (b) stoichiometry factor of O to Zn and Mn

Sample	**at(%)**			**Comments**	
	Zn	O	Mn	(a): $\frac{[Mn]}{[Mn+Zn]} \times 100$	(b): $\frac{[O]}{[Mn+Zn]}$
ZnO	34.00	66.00	0.00	0.00	1.94
***ZnMnO*@800°C**	22.30	74.04	3.65	14.07	2.85

ions. These findings not only corroborate the Mn^{2+} oxidation state but also affirm the successful substitution of Mn^{2+} ions into the Zn site positions within the ZnO lattice. Furthermore, higher binding energy peaks at 642.55 eV and 654.60 eV are unequivocally assigned to Mn^{3+} ions present in the ZnMnO thin film. The coexistence of two charge states, Mn^{+2} and Mn^{+3}, in Mn-doped ZnO has also been reported in previous studies [59, 60], further validating the observed Mn^{3+} peaks. Additionally, the presence of two satellite peaks, located around 645.32 eV and 657.15 eV, can be attributed to the electron shake-up of Mn^{2+}.

Figure 4(d) presents the high-resolution oxygen 1s signal, showcasing a binding energy of 530.65 eV for the annealed ZnMnO sample. Notably, the O 1s peak undergoes asymmetry upon Mn doping but regains its symmetrical shape following UHV treatment. Deconvolution of the O 1s peak in untreated ZnMnO, as illustrated in Figure 5(b), re-

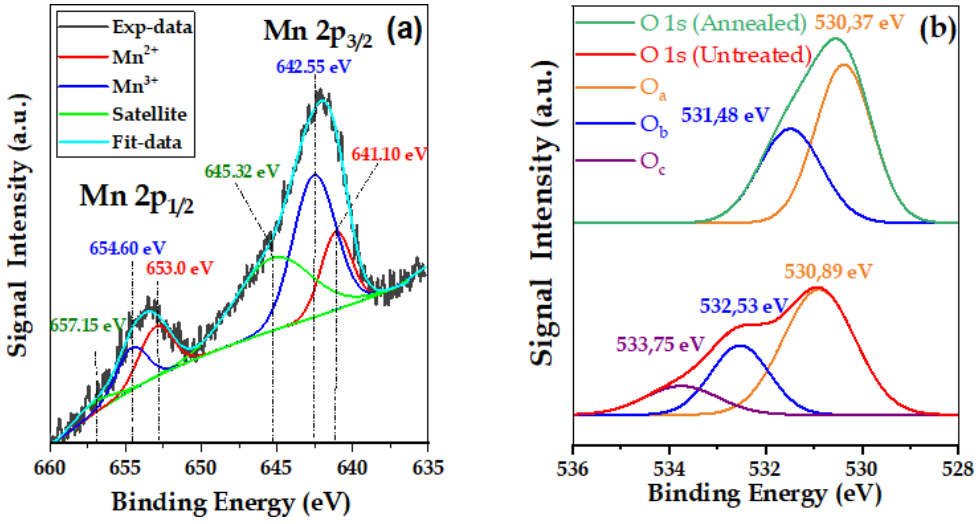

Fig. 5. Gaussian deconvolution of high-resolution XPS spectrum of: (a) doubled Mn 2p corresponding to treated *ZnMnO*(final state); and (b) O 1s corresponding to *ZnMnO* (untreated, annealed)

veals three distinct Gaussian peaks labeled as a, b, and c. The low binding energy peak O_a, located at 530.89 eV, corresponds to O^{2-} ions participating in Zn-O and/or Mn-O bonds. The intermediate binding energy peak O_b, observed at 532.53 eV, is associated with Zn-OH species. Additionally, the high binding energy peak O_c, appearing at 533.75 eV, is attributed to chemisorbed oxygen contributing to the formation of H_2O, CO_2, and/or oxygen defects such as V_o or O_i species, as previously reported [61, 62]. Upon the removal of contaminated layers containing OH, COx, and H_2O species through Ar ion sputtering and high-temperature annealing treatment, the Gaussian fit of the O 1s peak reveals only two sub-peaks, O_a and O_b, positioned at 530.37 eV and 531.48 eV, respectively [10, 14], showing considerable reduction in Vo or/and Zn_i concentrations.

4. Photoluminescence results

In this study, photoluminescence (PL) spectroscopy is utilized to investigate the impact of Mn incorporation and UHV treatment on the presence of defects. These defects subsequently alter the band gap and luminescence characteristics of zinc oxide [10, 19, 63].

Figure 6 shows the spectrum (i) related to pure ZnO. It exhibits two distinct emission bands. Firstly, a sharp ultraviolet (UV) emission at 3.27 eV (λ = 380 nm) is attributed to near band-edge emission (NBE) induced by free excitonic (F_x) radiative recombination. This emission is highly dependent on the crystalline quality [64]. Secondly, a broad visible emission ranging from 2.8 eV to 1.4 eV (λ = 442.86–885.70 nm), with a center at 2.26 eV (λ = 550 nm), is associated with intrinsic structural defects present in the optical band gap of ZnO [65]. These defects include zinc vacancies (V_{Zn}), oxygen vacancies (V_o), zinc interstitials (Zn_i), oxygen interstitials (O_i), and oxygen antisites (OZn).

Furthermore, Figure 6 (ii) illustrates three significant changes resulting from the incorporation of 4% Mn into the ZnO matrix: (1) The UV emission peak becomes more intense and broader compared to the undoped film. (2) The visible emission peak decreases. (3) There is a notable increase in the NIR (near infrared) emission peak at 1.65 eV. It is worth mentioning that the broadening of the NBE peak observed in spectrum (ii) aligns with the XRD findings, which indicate a broader FWHM for Mn-doped ZnO due to its inferior crystalline nature. The analysis of the PL spectrum further confirms the successful incorporation of Mn into the lattice.

Moreover, upon comparing spectra (ii) and (iii),

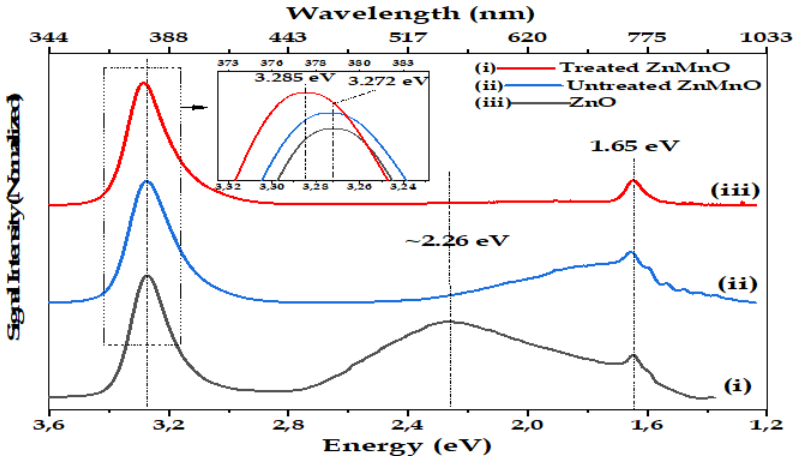

Fig. 6. PL spectra of pure ZnO (i), untreated ZnMnO (ii), and treated ZnMnO (iii)

it is evident that the UHV treatment provides several changes. Firstly, it facilitates the removal of the primary visible peak by completely eliminating the structural defects associated with O_i states and V_o, as discussed in the XPS results of O 1s. Secondly, it leads to the broadening of the UV emission peak, accompanied by a slight redshift of 0.013 eV. This shift is attributed to the band gap narrowing resulting from the strong interactions between the "s-p" electrons of Zn^{+2} ions and the "d" electrons of Mn^{+2} ions. Thirdly, it effectively eliminates the shoulder of the near-infrared emission peak caused by the presence of hydrogen impurity (Hi) at 1.65 eV (750 nm) [66]. Based on the aforementioned observations, we have established a connection between ZnO doping with Mn, UHV treatment, and their influence on the structural and photoelectronic properties. Furthermore, this study highlights the informative relationship between the XRD and XPS analysis techniques and the PL measurements.

For more clarification of modifications due to Mn doping and UHV treatment, Figure 7 gives a Gaussian deconvolution of the PL spectra corresponding to pure ZnO (i), untreated ZnMnO(ii), and treated ZnMnO(iii), accompanied by schematic band diagrams with the approximate positions of defect levels and luminescence mechanisms as suggested by other authors.

The NBE peak has been reported to include three sub-peaks. The first one at 3.275 eV (378 nm) concerns the free excitons (FX) from the state energy of 0.06 eV under the bottom of the conduction band minimum to the valence band maximum *(FX* $\rightarrow$ *VBM)* [67]. The second peak appears at 3.16 eV (392 nm), corresponding to the transitions from Zn_i states located at 0.15 eV under the bottom of the conduction band minimum (CBM) to the valence band maximum *(*$Zn_i \rightarrow$ *VBM)* [68]. The last peak is much less intense than the previous ones, at 3.03 eV (409 nm), corresponding to the transition from CBM to V_{Zn}-bound states located 0.27 eV above VBM (CBM $\rightarrow V_{Zn}$) [69]. It should be noted that this peak becomes more obvious with Mn-doped ZnO.

The broad visible emission was found to be fitted with four Gaussian subpeaks positioned at 2.50, 2.28, 2.05, and 1.80 eV for pure ZnO. Figure 7 shows a noticeable shift in the position peaks and clear variations in the relative intensities when Mn substitutes Zn in the ZnO film. The blue luminescence centered at 2.50 eV (496 nm) originates from the transition of electrons between $V_{Zn}$and the CBM (CBM $\rightarrow V_{Zn}$) [70] and disappears completely for ZnMnO. The green and yellow luminescence centered at 2.28 (544) and 2.05 eV (605 nm), respectively, originates from the transition of electrons between CBM and the O_i (CBM $\rightarrow$ O_i) [71] and decreases notably for ZnMnO before disappearing completely after the UHV treatment. Finally, the transition from the state extended-Zn_i at 0.6 eV from the CBM to the state V_O at 0.9 eV

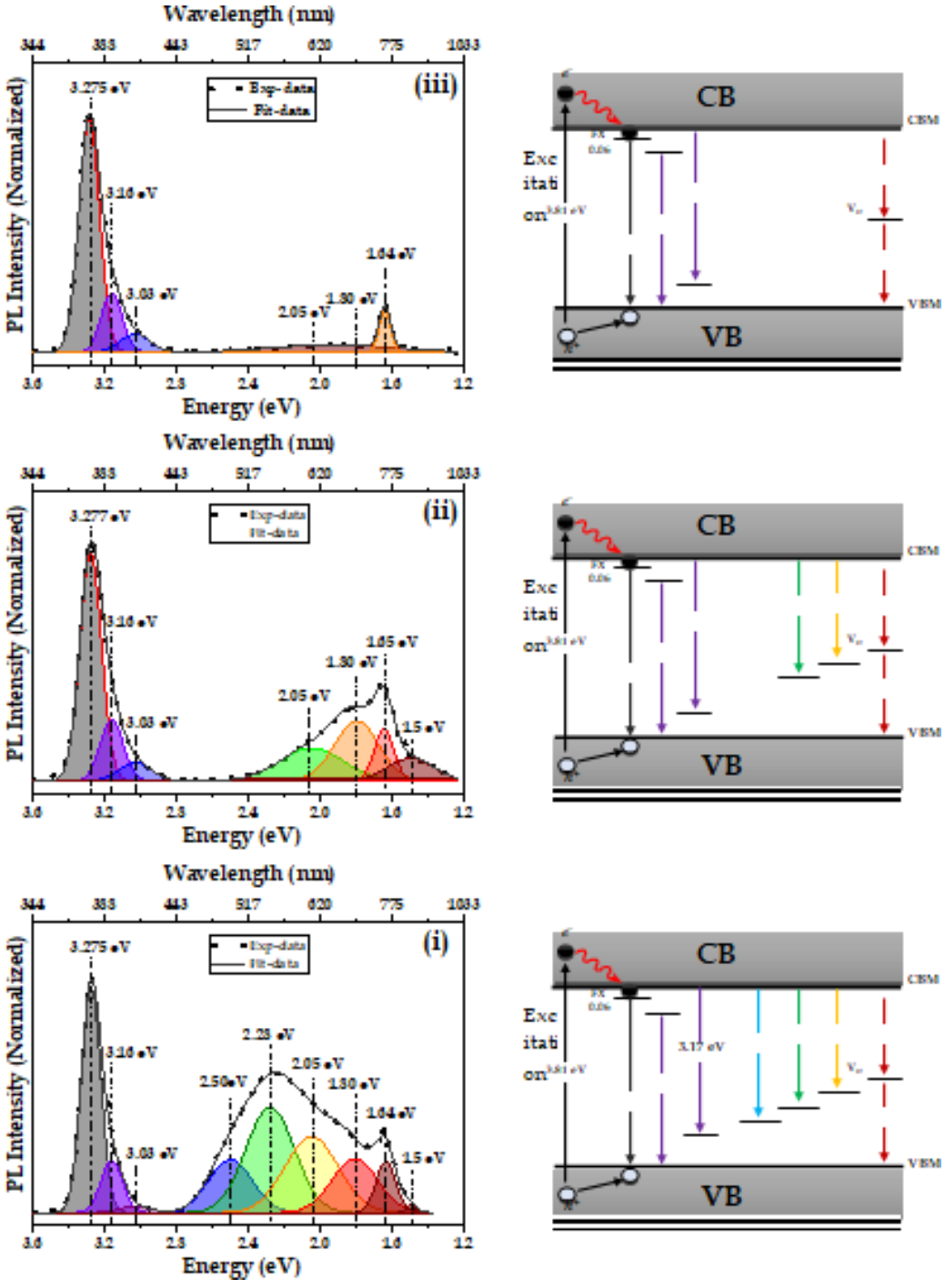

Fig. 7. Gaussian fitting of PL spectra accompanied by schematic band diagram corresponding to pure ZnO (i), untreated ZnMnO (ii), and treated ZnMnO (iii)

above the VBM (ex-$Zn_i \rightarrow V_O$) is associated with the orange luminescence centered at 1.80 eV (689 nm) [72].

The near-IR luminescence shows two sub-peaks at 1.65 and 1.5 eV, respectively; the peak at 1.5 eV due to the hydrogen impurity (Hi) (Hi $\rightarrow V_O$) [73] is completely erased by the UHV treatment. This implies that the hydrogen impurity (Hi) has

been effectively removed; however, the other peak caused by the V_O defect is located in the middle of the bandgap (CBM $\rightarrow V_O$, $V_O \rightarrow$ VBM) [71, 74]. Controlled Mn doping of ZnO, according to the PL study, can improve its optical characteristics for uses beyond spintronics, such as optoelectronics.

5. Conclusion

The objective of this paper was to investigate the effects of low-level Mn substitution and the treatment process on the chemical, structural, morphological, and optoelectronic properties of ZnO and ZnMnO thin films with 3.6 at% Mn. The thin films were synthesized using the ultrasonic pyrolysis technique on Si (100) substrates, following a standardized deposition procedure. Analysis of the AFM images revealed significant changes in surface morphology attributed to the incorporation of Mn, leading to noticeable decreases in grain size, and increases in height,and average roughness. XRD analysis confirmed the presence of the würtzite crystal structure of ZnO, with the dominant (002) plane governing the growth process across all films. Furthermore, slight reductions and shifts towards lower diffraction angles in the XRD peaks, accompanied by minor variations in lattice parameters and an increase in micro strain, provided compelling evidence supporting the successful integration of Mn^{2+} ions through Zn^{2+} substitution.

To gain deeper insights into the optical properties, XPS and PL spectroscopy were employed. The observed near band-edge emission (NBE) at 3.27 eV within the ultraviolet (UV) range, suppression of the yellow-orange, green emission (~2.6-1.8 eV), and the emergence of a distinct emission peak at 1.65 eV were identified as characteristic signatures associated with the presence of Mn atoms. Therefore, the above-mentioned results, in combination with the reduced grain size, improved micro-stain deformations, and decreased ionization potential, facilitated the accurate reproduction of the diagrams representing both ZnO and ZnMnO compounds. This is both before and after UHV treatment and annealing. It is worth noting that the structural defects responsible for visible emissions were effectively eliminated in ZnMnO, resulting in well-defined emissions confined solely to the near-infrared and ultraviolet ranges.

Acknowledgements

We acknowledge Materials Laboratory "LABMAT" ENP–Oran of Algeria for supporting this work, and "CRAPC," a scientific and technical research center in physico-chemical analysis (Bejaia).

References

[1] Kang Y, Yu F, Zhang L, Wang W, Chen S, Li Y. Review of ZnO-based nanomaterials in gas sensors. Solid State Ion. 2021;360: 115544.doi.org/10.1016/j.ssi.(2020).115544

[2] Bui DP, Pham MT, Tran HH, Nguyen TD, Cao TM, Pham VV. Revisiting the key optical and electrical characteristics in reporting the photocatalysis of semiconductors, ACS Omega. 2021;6:27379–86. doi:10.26434/chemrxiv-2021-bs8xg

[3] Bousmaha M, BezzerroukMA, Kharroubi B, Akriche A, Naceur R, Hattabi I, Sandjak-Eddine K. Enhanced photocatalysis by depositing ZnO thin film in the inner wall of glass tube. Optik. 2019;183:727–31. doi:10.1016/j.ijleo.2019.02.111

[4] Liu S, Zhong Q, Guo W, Zhang W, Ya Y, Xia Y. Novel Platycladusorientalis–shaped Fe-doped ZnO hierarchical nanoflower decorated with Ag nanoparticles for photocatalytic application. J. Alloys Compd. 2021; 880:160501. doi: 10.1016/j.jallcom.2021.160501

[5] Bezzerrouk MA, Bousmaha M, Hassan M, Akriche A, Kharroubi B, Naceur R. Enhanced methylene blue removal efficiency of SnO_2 thin film using sono-photocatalytic processes, Opt. Mater. 2021;117: 111116. doi:10.1016/j.optmat.2021.111116

[6] Aadnan I, Zegaoui O, ElMragui A, Daou I, Moussout H, Esteves da Silva JCG. Structural, optical and photocatalytic properties of Mn doped ZnO nanoparticles used as photocatalysts for Azo-dye degradation under visible light. Catalysts. 2022;12:1382. doi.org/10.3390/catal1211138

[7] Klein A, Körber C, Wachau A, Säuberlich F, Gassenbauer Y, Harvey SP, Proffit DE, Mason TO. Transparent conducting oxides for photovoltaics: manipulation of fermi level, work function and energy band alignment. Materials. 2010;3:4892–914. doi:10.3390/ma3114892

[8] IShaheen I, Ahmad KS, Zequine C, Gupta RK, Thomas AG, Malik MA. Facile ZnO-based nanomaterial and its fabrication as a supercapacitor electrode: synthesis, characterization and electrochemical studies. RSC Adv. 2021; 11:23374, doi: 10.1039/d1ra04341b

[9] Jin C, Hao N, Xu Z, Trase I, Nie Y, Dong L, Closson A, Chen Z, Zhang JXJ. Flexible piezoelectric nanogenerators using metal-doped ZnO-PVDF films. Sens. Actuators A Phys. 2020;305:111912. doi.org/10.1016/j.sna.2020.111912

[10] Stara TR, Markevich IV. Influence of Mn doping on ZnO defect-related emission. Semicond Phys Quantum Electron Optoelectro. 2017;20(1):137–41. doi.org/10.15407/spqeo20.01.137

[11] Pradeev Raj K, Sadaiyandi K, Kennedy A, Sagadevan S, Chowdhury ZZ, Johan MRB, Aziz FA, Rafique RF, Thamiz Selvi R, Rathina Bala R. Influence of Mg Doping on ZnO Nanoparticles for Enhanced Photocatalytic Evaluation and Antibacterial Analysis. Nanoscale Res Lett. 2018 Aug 3;13(1):229. doi: 10.1186/s11671-018-2643-x.

[12] Hou Q, Liu Y. Effects of Co doping and point defect on the ferromagnetism of ZnO. J Supercond Nov Magn. 2019;*32*, 1135-42. doi:10.1007/s10948-018-4987-y

[13] Bedrouni M, Kharroubi B, Ouerdane A, Bouslama M, Caudano Y, Bensassi KB, Bousmaha M, Bezzerrouk MA, Mokadem A, Abdelkrim M. Effect of indium incorporation, stimulated by UHV treatment, on the chemical, optical and electronic properties of ZnO thin film. Opt. Mater. 2021;111:110560. doi.org/10.1016/j.optmat.2020.110560

[14] Guezzoul M, Bouslama M, Ouerdane A, Mokadem A, Kharroubi B, Bedrouni M, Abdelkrim A, Abdellaoui A, Bensassi KB, Baizid A, Halati MS. Morphological and optical properties of undoped and Cu-doped ZnO thin films submitted to UHV treatment. Appl Surf Sci. 2020;520:146302. doi: 10.1016/j.apsusc.2020.146302

[15] Nurfani E, Kesuma W, Lailani A, Anrokhi M, Kadja G, Rozana M, Sipahutar W, Arif M. Enhanced UV sensing of ZnO films by Cu doping. Opt Mater. 2021;114:110973. doi:10.1016/j.optmat.2021.110973

[16] Azizah N, Muhammady S, Purbayanto MAK, Nurfani E, Winata T, Sustini E, Widita R, Darma Y. Influence of Al doping on the crystal structure, optical properties, and photodetecting performance of ZnO film. Prog Nat Sci Mater Int. 2020;30:28–34. doi: 10.1016/j.pnsc.2020.01.006

[17] Sajjad M, Ullah I, Khan M, Khan J, Khan MY, Qureshi MT. Structural and optical properties of pure and copper doped zinc oxide nanoparticles. Results Physi 2018; 9:1301–9. doi: 10.1016/j.rinp.2018.04.010

[18] Kim D, Kim W, Jeon S, Yong K. Highly efficient UV-sensing properties of Sb-doped ZnO nanorod arrays synthesized by a facile, singlestep hydrothermal reaction. RSC Adv. 2017;7:40539.doi: 10.1039/c7ra07157d

[19] Abdelkrim M, Guezzoul M, Bedrouni M, Bouslama M, Ouerdane A, Kharroubi B. Effect of slight cobalt incorporation on the chemical, structural, morphological, optoelectronic, and photocatalytic properties of ZnO thin film. J. Alloys Compd. 2022;920:165703. doi.org/10.1016/j.jallcom.2022.165703

[20] Chen M, Liu P, He JH, Wang HL, Zhang H, Wang X, Chen R. Nanofiber template induced preparation of ZnO nanocrystal and its application in photocatalysis, Sci Rep. 2021;11:21196.doi.org/10.1038/s41598-021-00303-9

[21] Fathima N, Pradeep N, Balakrishnan VUJ. Growth and characterization of ZnO nanocones on flexible substrate by hydrothermal method. Mater Today Proc. 2019;9: 247–55. doi: 10.1016/j.matpr.2019.02.156

[22] Aravind A, Jayaraj M, ZnO-based dilute magnetic Ssemiconductors. In: Jayaraj MK, editor. Nanostructured metal oxides and devices. Singapore: Springer; 2020. p.233–69. doi: 10.1007/978-981-15-3314-3_8

[23] Pan F, Song C, Liu XJ, Yang YC, Zeng F. Ferromagnetism and possible application in spintronics of transition-metal-doped ZnO films. Mater Sci Eng R: Rep. 2008;62:1–35. doi: 10.1016/j.mser.2008.04.002

[24] RBaghdad R, Kharroubi B, Abdiche A, Bousmaha M, Bezzerrouk MA, Zeinert A, Marssi ME, Zellama K. Mn doped ZnO nanostructured thin films prepared by ultrasonic spray pyrolysis method. Superlattices Microstruct. 2012;52:711–21. doi.org/10.1016/j.spmi.2012.06.023

[25] Gallegos MV, Peluso MA, Thomas H, Damonte LC, Sambeth JE. Structural and optical properties of ZnO and manganese-doped ZnO, J. Alloys Compd. 2016;689:416–24.doi: 10.1016/j.jallcom.2016.07.283

[26] Alsmadi AKM, Salameh B, Shatnawi M. Influence of oxygen defects and their evolution on the Ferromagnetic ordering and band gap of Mn-doped ZnO films. J Phys Chem C. 2020;124:16116–26, doi.org/10.1021/acs.jpcc.0c04049

[27] Ilyas U, LeejP, Tan TL, Chen R, Anwar AW, Zhang S, Sun HD, Rawat RS. Temperature-dependent stoichiometric alteration in ZnO:Mn nanostructured thin films for enhanced ferromagnetic response. Appl Surf Sci. doi.org/10.1016/j.apsusc.2016.06.138

[28] Jing C, Jiang Y, Bai W, Chu J, Liu A. Synthesis of Mn-doped ZnO diluted magnetic semiconductors in the presence of ethyl acetoacetate under solvothermal conditions. J Magn Magn Mater. 2010;322:2395–400.doi:10.1016/j.jmmm.2010.02.044

[29] Panda J, Sasmal L, Nath TK. Magnetic and optical properties of Mn doped ZnO vertically aligned nanorods synthesized by hydrothermal technique. AIP Adv. 2016;6:035118.doi.org/10.1063/1.4944837

[30] Rajendran K, Banerjee S, Senthilkumaar S, Chini TK, Sengodan V. Influence of Mn doping on the microstructure and optical property of ZnO. Mater. Sci. Semicond. 2008;11:6–12. doi:10.1016/j.mssp.2008.04.005

[31] Hajiashrafi S, Motakef Kazem I N. Preparation and evaluation of ZnO nanoparticles by thermal decomposition of MOF-5. Heliyon 2019;5:1–6.doi: 10.1016/j.heliyon.2019.e02152.

[32] Mikailzade F, Türkan H, Önal F, Zarbali M, Göktaş A, Tumbul A. Structural and magnetic properties of polycrystalline $Zn_{1-x}Mn_xO$ films synthesized on glass and p-type Si substrates using Sol–Gel technique. Appl Phys A. 2021;127:1–8. doi: 10.1007/s00339-021-04519-4

[33] Shewale P, Lee S, Yu S. UV sensitive pulsed laser deposited ZnO thin films: influence of growth temperature. J Alloys Compd. 2018;744:849–58. doi: 10.1016/j.jallcom.2018.02.141

[34] Pereira dos Santos CI, De Giovanni Rodrigues A, Franco

de Godoy MP. Growth and characterization of Mn-doped ZnO thin films.18th Brazilian Workshop on Semiconductor Physics BWSP. 2017. doi: 10.17648/bwsp-2017-70009

[35] Wang J, Mei Y, Lu X, Fan X, Kang D, Xu P, Tan T. Effects of annealing pressureand Ar+ sputtering cleaning on Al-doped ZnO films. Appl Surf Sci. 2016;387:779–83. doi.org/10.1016/j.apsusc.2016.06.069

[36] Sun LJ, He DK, Xu SQ, Zhong Z, Wu XP, Lin BX, Fu ZX, Effect of hightemperature annealing on conduction-type ZnO films prepared by direct-current magnetron sputtering. Chin Phys Lett. 2010;27(12):126802. doi: 10.1088/0256-307X/27/12/126802

[37] Chang HY, Lin WC, Chu PC, Wang YK, Sogo M, Iida SI, Peng CJ, Miyayama T. Xray photoelectron spectroscopy equipped with gas cluster ion beams for evaluation of the sputtering behavior of various nanomaterials. ACS Appl Nano Mater. 2022. doi.org/10.1021/acsanm.2c00202

[38] Zaiter A, Michon A, Nemoz N, et al. Crystalline Quality and Surface Morphology Improvement of Face-to-Face Annealed MBE-Grown AlN on h-BN, Materials. 2022; 15(23):8602. doi.org/10.3390/ma1523860

[39] ArzuÇolak, HW, Zandvliet HJW, Poelsema B. Surface adhesion and its dependence on surface roughness and humidity measured with a flat tip. Appl Surf Sci. 2012;69:6938.doi.org/10.1016/j.apsusc.2012.03.138

[40] Yang S, Yan B, Lu L, Zeng K. Grain boundary effects on Li-ion diffusion in a Li1.2Co0.13Ni0.13MnO.54O2 thin film cathode studied by scanning probe microscopy technique. RSC Adv. 2016;6:94000.doi: 10.1039/c6ra17681j

[41] Pathak CS. Application of atomic force microscopy in organic and perovskite photovoltaics. In: Pathak CS, Kumar S, editors. Recent developments in atomic force microscopy and raman spectroscopy for materials characterization. book London, UK: IntechOpen; 2021. doi: 10.5772/intechopen.98478

[42] Mikhailov YM, Aleshin VV, Kolesnikova AM, Kovalev DY, Ponomarev VI. Flameless combustion synthesis of Ni and Ag nanoparticles in ballasted systems: atime-resolved X-ray diffraction study. Propellants Explos Pyrotech. 2015;40:88. doi: 10.1002/prep.201400049

[43] Murata K, Chihara H, Tsuchiyama A, Koike C, Takakura T, Noguchi T, Nakamura T. Crystallization experiments on amorphous silicates with chondritic composition: Quantitative formulation of the crystallization. Astrophys J. 2007;668:285. doi:10.1086/521017

[44] Niedermaier I, Kolbeck C, Steinrück HP, Florian M. Dual analyzer system for surface analysis dedicated for angle-resolved photoelectron spectroscopy at liquid surfaces and interfaces. Rev Sci Instrum. 2016;87:045105. doi.org/10.1063/1.4942943

[45] Motaung DE, Kortidis I, Papadaki D, Nkosi SS, Mhlongo GH, Wesley-Smith J, Malgas GF, Mwakikunga BW, Coetsee E, Swart HC, Kiriakidis G, Ray SS. Defect-inducedmagnetism in undoped and Mn-doped wide band gap zinc oxidegrown by aerosol spray pyrolysis. Appl Surf Sci. 2014;311:14–26. doi: 10.1016/j.apsusc.2014.04.183

[46] Wang XL, Luan CY, Shao Q, Pruna A, Leung CW, Lortz R, Zapien JA, Ruotolo A. Effect of the magnetic order onthe room-temperature band-gap of Mn-doped ZnO thin films. Appl Phys Lett. 2013;102:102112. doi: 10.1063/1.4795797

[47] Eckelt F, Rothweiler P, Braun F, Voss L, AnkicaŠari, MV, Lützenkirchen-Hecht D. In situ observation of ZnO nanoparticle formation by a combination of time-resolved X-ray absorption spectroscopy and X-ray diffraction. Materials. 2022;15:8186.doi.org/10.3390/ma15228186

[48] Ahmed N, Majid A, Khan MA, Rashidi M, Umar ZA, Baig MA. Synthesis and characterization of Zn/ZnO microspheres on indented sites of silicon substrate. Mater Sci-Pol. 2018;36(3):501–8.doi: 10.2478/msp-2018-005

[49] Sahu S, Samanta PK. Peak profile analysis of X-ray diffraction pattern of zinc oxide nanostructure, J Nano Electron Phys. 2021;13:1–4.doi:10.21272/jnep.13(5).05001

[50] Das A, Wary RR, Nair RG. Mn-doped ZnO, role of morphological evolution on enhanced photocatalytic performance. Energy Rep. 2020;6:737–41. doi.org/10.1016/j.egyr.2019.11.148

[51] Rekha K, et al. Structural, optical, photocatalytic and antibacterial activity of zinc oxide and manganese doped zinc oxide nanoparticles. Phys B: Condensed Matter 2010405(15):3180–5. doi: 10.1016/j.physb.2010.04.042

[52] Gencer H, Goktas A, Gunes M, Mutlu H, Atalay S. Electrical transport and magnetoresistance properties of La0.67Ca0.33MnO3 film coated on pyrex glass substrate. Int J Mod Phys B. 2008;22:497–506. doi: 10.1142/S0217979208038776

[53] Vishwaroop R, Mathad SN. Synthesis, structural, WH plot and size-strain analysis of nano cobalt doped $MgFe_2O_4$ ferrite. Sci Sinter. 2020;52:349.doi: 10.2298/SOS2003349V

[54] Salameh B, Alsmadi A, Shatnawi M. Effects of Co concentration and annealingon the magnetic properties of Co-doped ZnO films: role of oxygen vacancies on theferromagnetic ordering, J. Alloys Compd. 2020;835:155287. doi: 10.1016/j.jallcom.2020.155287

[55] Tarwal N, Gurav K, Kumar TP, Jeong Y, Shim H, Kim I, Kim J, Jang J, Patil P. Structure, X-ray photoelectron spectroscopy and photoluminescence investigations of the spray deposited cobalt doped ZnO thin films. J Anal Appl Pyrolysis. 2014;106:26–32. doi: 10.1016/j.jaap.2013.12.005

[56] Toloman D, Mesaros A, Popa A, Raita O, Silipas TD, Vasile BS, Pana O, Giurgiu LM. Evidence by EPR of ferromagnetic phase in Mn-doped ZnO nanoparticles annealed at different temperatures. J. Alloys Compd. 2013;551:502–7. doi: 10.1016/j.jallcom.2012.10.183

[57] Kasim MF, Darman AKAB, Yaakob MK, Badar N, Kamarulzaman N. Experimental and first-principles

DFT studies on the band gap behaviours of microsized and nanosized Zn(1-x)MnxO materials. Phys Chem Chem Phys. 2019;21:19126–19146. doi: 10.1039/C9CP01664C

[58] Ianhez-Pereira C, Onofre YJ, Magon CJ, et al. The interplay between Mn valence and the optical response of ZnMnO thin films. Appl Phys A. 2020;126:337. doi.org/10.1007/s00339-020-03511-8

[59] Guo D, Wu Z, An Y, Li X, Guo X, Chu X, Sun C, Lei M, Li L, Cao L, Li P, Tang W. Room temperature ferromagnetism in (Ga1-x Mnx)$2O_3$ epitaxial thin films. J Mater Chem C. 2015;3:1830–4. doi.org/10.1039/C4TC02833C

[60] Ramírez A, Hillebrand P, Stellmach D, May MM, Bogdanoff P, Fiechter S. Evaluation of MnOx, Mn_2 O_3, and Mn_3O_4 electrodeposited films for the oxygen evolution reaction of water. J Phys Chem C. 2014;118:14073–81.doi.org/10.1021/jp500939d

[61] Yang S, Zhang Y. Structural, optical and magnetic properties of Mn-doped ZnO thin films prepared by Sol-Gel method. J Magn Magn Mater. 2013;334:52–8. doi: 10.1016/j.jmmm.2013.01.026

[62] Gao Q, Dai Y, Li C, Yang L, Li X, Cui C. Correlation between oxygen vacancies and dopant concentration in Mn-doped ZnO nanoparticles synthesized by co-precipitation technique. J. Alloys Compd. 2016;684:669–76. doi: 10.1016/j.jallcom.2016.05.227

[63] Velavan R, Balakrishnan G, Batoo KM, Raslan EH. Synthesis and characterization of pure and manganese (Mn) doped zinc oxide (ZnO) nanocrystallites for applications. J Civil Environ Eng. 2021;11:1–4

[64] Wang XL, Luan CY, Shao Q, Pruna A, Leung CW, Lortz R, Zapien JA, Ruotolo A. Effect of the magnetic order on the room-temperature band-gap of Mn-doped ZnO thin films. Appl Phys Lett. 2013;102:102112. doi: 10.1063/1.4795797

[65] Zeng H, Duan G, Li Y, Yang S, Xu X, Cai W. Blue luminescence of ZnO nanoparticles based on non-equilibrium processes: defect origins and emission controls. Adv. Funct. Mater. 2010;20:561–72. doi: 10.1002/adfm.200901884

[66] Bensassi KB, et al. A comparative study of un-doped ZnO and in doping ZnO thin films with various concentrations, subjected to appropriate UHV treatment and characterized by sensitive spectroscopy techniques XPS, AES, reels, and PL. Ann W Univ Timisoara-Phys. 2022;64(1):1–21. doi: 10.2478/awutp-2022-0001

[67] Haiping H, et al. Extraction of the surface trap level from photoluminescence: a case study of ZnO nanostructures. Phys Chem Chem Phys. 2011;13(33):14902. doi: 10.1039/c1cp21527b

[68] Iribarren A, et al. Elucidating room-temperature optical transitions in annealed ZnO nanoparticles synthesized from an aqueous method. Mater Res Expr. 2019;6(10):105048. doi: 10.1088/2053-1591/ab3865

[69] Djurisic AB, Choy WCH, Roy VAL, Leung YH, Kwong CY, Cheah KW, Gundu Rao TK, Chan WK, Lui HF, Suryu C. Photoluminescence and electron paramagnetic resonance of ZnO tetrapod structures. Adv Func Mater. 2004;14:856. doi: 10.1002/adfm.200305082

[70] Mhlongo GH, et al. Room temperature ferromagnetism and gas sensing in ZnO nanostructures: influence of intrinsic defects and Mn, Co, Cu doping. Appl Surf Sci. 2016;390:804–15. doi: 10.1016/j.apsusc.2016.08.138

[71] Xu Y, et al. Passivation effect on ZnO films by SF6 plasma treatment. Crystals. 2019;9(5):236. doi: 10.3390/cryst9050236

[72] Lee SH, et al. Inorganic nano light-emitting transistor: p-type porous silicon nanowire/n-type ZnO nanofilm. Small. 2016;12(31):4222–8. doi: 10.1002/smll.201601205

[73] Djurišić AB, et al. ZnO nanostructures: growth, properties and applications. J Mater Chem. 2012;22(14):6526–35.doi.org/10.1039/C2JM15548F

[74] Fernando S, Nilius N, Freund HJ. STM luminescence spectroscopy of intrinsic defects in ZnO (0001) thin films. J Phys Chem Lett. 2013;4(22):3972–6. doi: 10.1021/jz401823c

Received 2023-03-22
Accepted 2023-09-17